Marine and Petroleum Geology 88 (2017) 932–949

Contents lists available at ScienceDirect

Marine and Petroleum Geology

journal homepage: www.elsevier.com/locate/marpetgeo

Research paper

Effect of pore structure on shale oil accumulation in the lower third member of the Shahejie formation, Zhanhua Sag, eastern China: Evidence from gas adsorption and nuclear magnetic resonance

Tingwei Li [a, b], Zhenxue Jiang [a, b, *], Chenlu Xu [c, d, **], Bo Liu [e], Guoheng Liu [a], Pengfei Wang [f], Xin Li [a, b], Weitao Chen [a, b], Chuanxiang Ning [g], Zhi Wang [a, b]

[a] State Key Laboratory of Petroleum Resources and Prospecting, China University of Petroleum, Beijing 102249, China
[b] Unconventional Natural Gas Research Institute, China University of Petroleum, Beijing 102249, China
[c] Key Laboratory of Petroleum Resource Research, Institute of Geology and Geophysics, Chinese Academy of Sciences, Beijing 100029, China
[d] University of Chinese Academy of Sciences, Beijing 100049, China
[e] Accumulation and Development of Unconventional Oil and Gas, State Key Laboratory Cultivation Base Jointly-constructed by Heilongjiang Province and Ministry of Science and Technology, Northeast Petroleum University, Daqing 163318, China
[f] Geoscience Documentation Center, China Geological Survey, Beijing 10083, China
[g] Wuxi Research Institute of Petroleum Geology, Sinopec Petroleum Exploration & Production Research Institute, Wuxi 214126, China

ARTICLE INFO

Article history:
Received 21 July 2017
Received in revised form
27 September 2017
Accepted 28 September 2017
Available online 30 September 2017

Keywords:
Zhanhua Sag
Es_3^l member
Pore structure
Shale oil accumulation
Gas adsorption
Nuclear magnetic resonance

ABSTRACT

As shale oil occurs primarily in micro–nano pores and fractures, research about the effect of pore structure on shale oil accumulation has great significance for shale oil exploration and development. The effect of pore structure on shale oil accumulation in the lower third member of the Shahejie formation (Es_3^l), Zhanhua Sag, eastern China was investigated using gas adsorption, soxhlet extraction, nuclear magnetic resonance (NMR) analysis, and field emission scanning electron microscope (FE-SEM) observation. The results indicated that the samples contained a larger amount of ink-bottle-shaped and slit-shaped pores after extraction than before extraction. The pore volume and specific surface area of the samples were approximately 2.5 times larger after extraction than before extraction. Residual hydrocarbon occurred primarily in the free-state form in pores with diameters of 10–1000 nm, which can provide sufficient pore volume for free hydrocarbon accumulation. Therefore, pores with diameters of 10–1000 nm were regarded as "oil-enriched pores", which are effective pores for shale oil exploration, whereas pores with diameters smaller than 10 nm were regarded as "oil-ineffective pores". Samples with only well-developed small pores with diameters smaller than 1000 nm showed high oil saturation, whereas samples with both small pores and also relatively large pores and micro-fractures presented low oil saturation. As the minimum pore size allowing fluid expulsion is 1000 nm, pores with diameters greater than 1000 nm were considered as "oil-percolated pores". Large pores and micro-fractures are generally interconnected and may even form a complex fracture mesh, which greatly improves the permeability of shale reservoirs and is beneficial to fluid discharge.

© 2017 Published by Elsevier Ltd.

1. Introduction

The first commercial production of natural gas in the United States (1821) was from an organic-rich Devonian shale in the Appalachian Basin (Curtis, 2002). Although production from shale was limited for many decades, shale oil and gas have recently become important energy sources in North America (Montgomery et al., 2005; Jarvie et al., 2007; Chalmers and Bustin, 2008; Ross and Bustin, 2008). The great success of shale oil and gas production in North America has aroused widespread interest across the world. In recent years, petroleum scientists in China have initiated research on shale oil and gas, which have gradually become important targets for oil and gas exploration (Jiang et al., 2012; Guo, 2014; Wang, 2015; Li et al., 2017b).

* Corresponding author. No. 18 Fuxue Road, Changping, Beijing, China.
** Corresponding author. No.19 Beitucheng Western Road, Chaoyang, Beijing, China.
E-mail addresses: zhenxuejiang@163.com (Z. Jiang), xcl@mail.iggcas.ac.cn (C. Xu).

https://doi.org/10.1016/j.marpetgeo.2017.09.030
0264-8172/© 2017 Published by Elsevier Ltd.

Shale oil refers essentially to the liquid hydrocarbon that is enriched in micro–nano pores and fractures in organic-rich shale, which occurs in the free, adsorbed, and dissolved states (Curtis, 2002; Jarvie et al., 2007; Ji et al., 2015). Before the potential of oil production from shale was revealed by the shale-oil boom, organic-rich shale had always been considered as source rock in the exploration and development of conventional oil, which means that shale oil is the left-behind hydrocarbon that could not be expelled into adjacent conventional reservoirs (Li et al., 2015b). This "left-behind" hydrocarbon naturally remains in micro–nano pores and fractures of shale reservoirs, such as micropores (<2 nm), mesopores (2–50 nm), and macropores (>50 nm) (Tang et al., 2016; Wang et al., 2016; Li et al., 2017a). The practical exploration and development of shale oil demonstrated that micro–nano pore structure, such as pore size, volume, specific surface area, shape, and connectivity, played an extremely important role in the enrichment and percolation of shale oil (Javadpour et al., 2007; Haroonabadi and Haghifam, 2013; Ji et al., 2014; Li et al., 2015b; Pan et al., 2015). Li et al. (2015b) analysed the relationship between pore volume and oil content of the Qingshankou shale in the northern Songliao Basin and stated that the oil content of shale samples was controlled by only larger pores such as mesopores and macropores. On the contrary, Pan et al. (2015) performed an analysis of the Upper Permian Dalong shale in the northwestern margin of the Sichuan Basin and revealed that residual organic matter in shale samples occurred in micropores and small mesopores.

In recent years, many advanced techniques have been used to study the micro–nano pore structure of shale reservoirs (Chalmers and Bustin, 2007; Ross and Bustin, 2007, 2009; Clarkson et al., 2013; Li et al., 2016), and low-pressure adsorption and nuclear magnetic resonance have become two commonly used methods. Low-pressure adsorption can measure the pore volume, specific surface area, and pore size distribution (PSD) in shale reservoirs using CO_2 and N_2 as adsorbates (Chen et al., 2011, 2016; Clarkson et al., 2013; Mastalerz et al., 2013). Because CO_2 is able to enter 0.35 nm pores, CO_2 adsorption is used primarily to obtain the distribution characteristics of micropores (Cui et al., 2010; Chalmers et al., 2012; Tian et al., 2012). It is generally known that capillary condensation must be used to calculate PSD with N_2 adsorption (De Boer and Lippens, 1964; Rouquerol et al., 1994). Capillary condensation can occur only when the relative pressure is greater than 0.35 (Sing et al., 1985; Kondo et al., 2006). According to the Kelvin Equation, the larger the pore is, the higher the relative pressure required for capillary condensation is. When capillary condensation occurs in large pores, the relative pressure is close to the saturated vapour pressure, which is difficult to measure in an experiment. Therefore, N_2 adsorption cannot finely characterise parts of micropores, relatively large pores, and micro-fractures within shale (Li et al., 2015b; Tang et al., 2016), which have upper and lower limits as measured in this study of 300 nm and 2 nm, respectively.

NMR analysis can obtain the characteristics of pore structure and fluid distribution in shale reservoirs using the NMR phenomenon, and it has advantages in studying shale reservoirs because of its characteristics of being rapid, non-damaging and accurate (Brai et al., 2007; Saidian and Prasad, 2015; Xu et al., 2015; Li et al., 2016; Mehana and El-Monier, 2016). When samples containing fluid are in a uniform static magnetic field, hydrogen protons in the fluid are polarised, generating a magnetic vector. At this time, the hydrogen protons are stimulated by a frequency pulse to produce the NMR phenomenon. After removing the frequency pulse, a signal with amplitude that attenuates with time can be obtained. Generally, a transverse relaxation time (T_2) spectrum can be used to measure the attenuation rate of the nuclear magnetic signal, which is utilised to study shale characteristics (Coates et al., 1999; Wang, 2009; Sun et al., 2012; Li et al., 2016). According to the basic principle of NMR, there is a positive correlation between the T_2 of hydrogen protons in the pore water and the pore size (Kleinberg et al., 1993; Dunn et al., 2002; Yao et al., 2010a, b; Sun et al., 2012; Huang et al., 2015; Tan et al., 2015), specifically, the T_2 distributions reflect the PSD: small pores have short relaxation time, whereas large pores and micro-fractures have long relaxation time (Li et al., 2016). Moreover, the amplitude of the T_2 spectrum reflects the proportion of pores with different diameters in shale. That is, the stronger the T_2 spectrum amplitude is, the more developed pores with its corresponding diameters are. The T_2 measured by NMR analysis is normally between 0.01 and 1000 ms, corresponding to the pore size range of 1–100,000 nm (Li et al., 2016). Therefore, NMR can finely characterise parts of large pores and micro-fractures within shale samples.

The Es_3^l member in the Zhanhua Sag is the main set of lacustrine shale-oil producing series in eastern China. Many studies of the Es_3^l shale have been carried out, and these concentrate mainly on the basic features of the shale reservoirs, such as mineral composition, porosity, and permeability (Song et al., 2011; Liu et al., 2012; Wang et al., 2013a; Li et al., 2015a). However, research on the pore structure is relatively limited in the study area, and there is a particular paucity of research about the effect of pore structure on shale oil accumulation. Therefore, the aim of this study was to clarify the effect of pore structure on shale oil accumulation based on the methods of low-pressure gas adsorption, soxhlet extraction, NMR analysis, and FE-SEM, thus providing a scientific basis for shale oil exploration and development.

2. Geological setting and samples

The Zhanhua Sag is located in the northeastern Jiyang Depression, Bohai Bay Basin, eastern China (Fig. 1). It covers an area of 2800 km^2 and is located north of the Chenjiazhuang Uplift and west of the Kendong Uplift. Its western and northern sides are bounded by the Yidong Fault and the Chengdong Fault, respectively. The tectonic units in the Zhanhua Sag include the Gubei Sag, Bonan Sag, Gunan Sag, Fulin Sag, Sikou Sag, Kenxi Sag, and Gudao Uplift. Faults are well-developed in the Zhanhua Sag and include three major NW-trending faults, the Luoxi Fault, Guxi Fault, and Wuhaozhuang Fault, and a series of NE- and EW-trending faults (Zhang et al., 2005; Wang and Hu, 2014; Li et al., 2015a).

The Zhanhua Sag includes a very thick sequence of Cenozoic strata (Fig. 2). Paleogene shale occurs principally in the Shahejie formation (Song et al., 2015). The Es_3^l member is a major horizon of shale deposition and is a favourable horizon for shale oil production. Many wells have been drilled through the shale reservoirs in the Es_3^l member and have produced high-yielding commercial oil flows (Liu et al., 2012; Zhao et al., 2012; Wang et al., 2013b).

Because strong movement along the major faults resulted in crustal extension, basin subsidence, and increased water depth, the sedimentation period of the Es_3^l member in the Zhanhua Sag is considered to be the main period of source rock deposition. The lithology is predominantly grey and dark-grey shale, with a small amount of siltstone, belonging to moderate–deep lacustrine facies (Wang, 2015).

For this study, 18 core samples were collected from the Es_3^l member in the Luo-69 well within the Zhanhua Sag (Fig. 1). The Luo-69 well is an exploratory well drilled through the Neogene Minghuazhen and Guantao formations and the Paleogene Dongying, Shahejie, and Kongdian formations (from top to bottom) (Fig. 2). The Es_3^l member, located at depths of 2910 m–3130 m in the Luo-69 well, is the interval of interest in this study. It is characterised by a high abundance of organic matter with total organic carbon (TOC) contents ranging from 0.52 wt.% to 9.32 wt.% (average of 3.00 wt.%). The kerogen in the Es_3^l shale contains predominantly

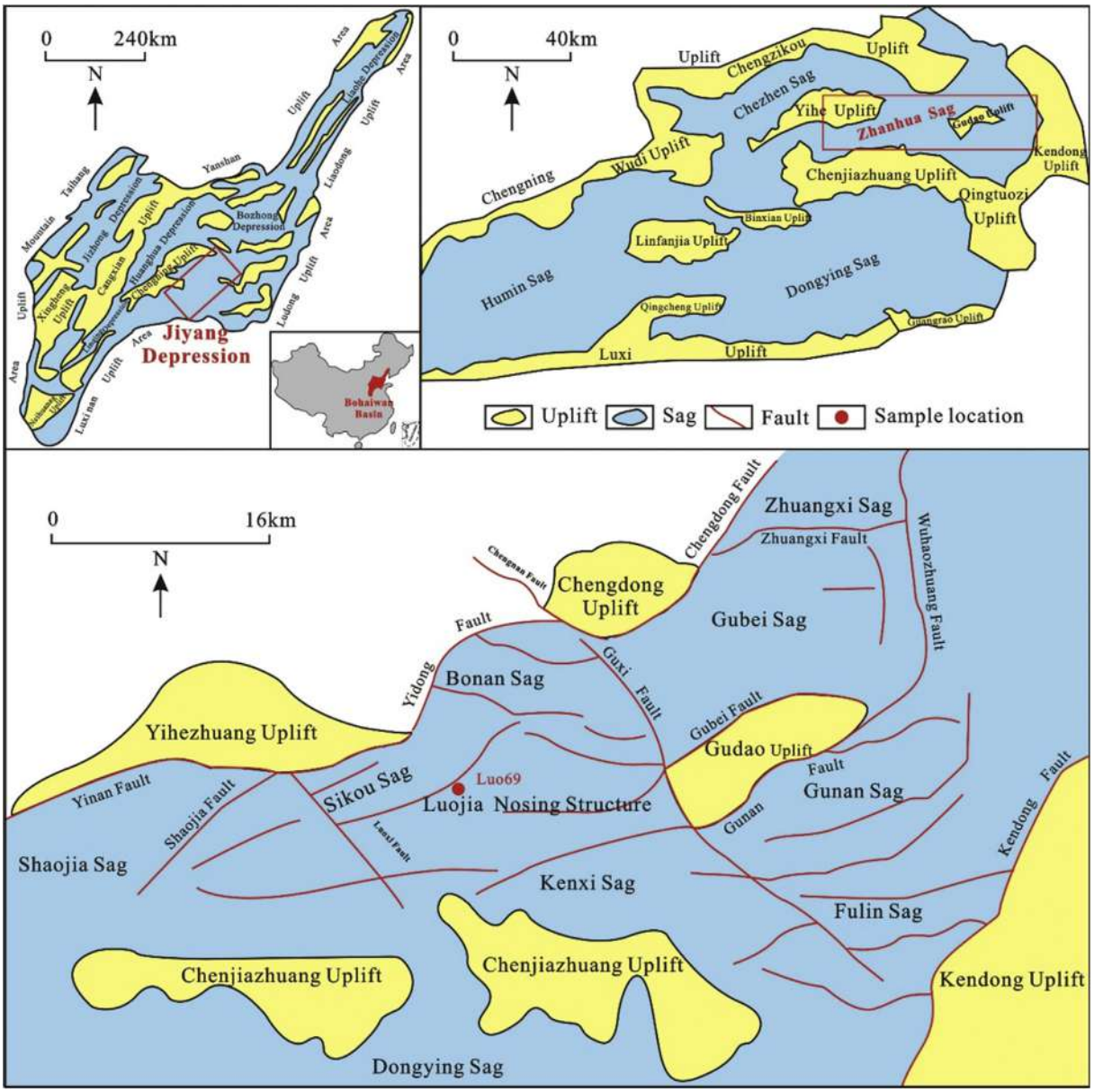

Fig. 1. Map of the study area in the Zhanhua Sag, Jiyang Depression, Bohai Bay Basin, eastern China.

Types I and II organic matter, presenting an incline to Type I and II_1. The Es_3^l shale is currently in the oil window and has vitrinite reflectance (Ro) values ranging from 0.70% to 0.91% (Li et al., 2017a, b). Therefore, the Es_3^l shale contains good materials for oil generation, and previous studies have proven that the Es_3^l shale has indeed generated a certain amount of hydrocarbons in its geological history (Liu et al., 2012; Wang et al., 2013b; Song et al., 2015).

3. Experimental methods

3.1. Gas adsorption and soxhlet extraction

Low-temperature low-pressure (77.15 K at 101.3 kPa) N_2 adsorption is a common method for characterising pore structure (Rouquerol et al., 1994). The specific surface area was obtained using the Brunauere–Emmette–Teller method (Brunauer et al., 1938). The PSD and pore volume were calculated using the Barrette–Joyner–Halenda theory (Brunauer et al., 1938; Barrett et al., 2014). Eight samples of shale were measured using a four-type automatic surface area and porosity physical adsorption instrument (Table 1). Each sample (approximately 1–2 g) was crushed into grains of 60–80 mesh size (180,000–250,000 nm) and automatically degassed at 383.15 K under vacuum for 14 h to remove adsorbed moisture and volatile matter before analysing with N_2.

CO_2 adsorption is more suitable for characterising the pore structure of micropores (Cui et al., 2010; Chalmers et al., 2012; Tian et al., 2012). Thus, the eight samples were used for CO_2 adsorption after the N_2 adsorption. Before the test, each sample was placed into a vacuum drying oven for 2 h for vacuumisation. The specific surface area was obtained using the CO_2 isothermal adsorption method at 273.15 K, whereas the PSD and pore volume were calculated using the Density Functional Theory model. Each sample was measured using a NOVA4200e specific surface area and pore-size distribution analyser.

Soxhlet extraction is a common method for extracting soluble organic matter from shale based on the theory of similarity and

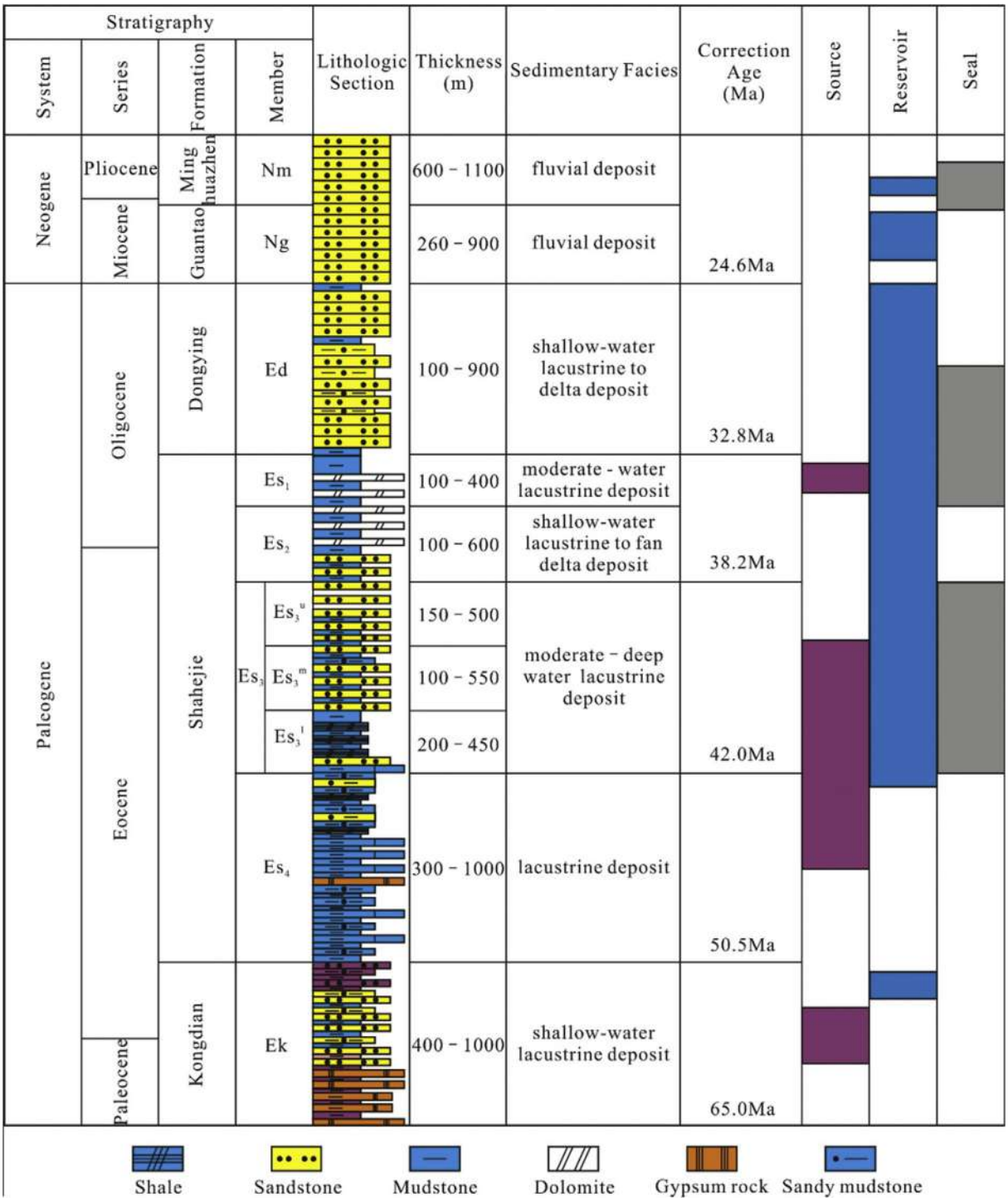

Fig. 2. Comprehensive stratigraphic column of the Jiyang Depression.

intermiscibility (Pan et al., 2015; Liu et al., 2016a, b; Xiong et al., 2016; Ji et al., 2017). After the N_2 and CO_2 adsorption, the eight shale samples were used for soxhlet extraction. Each sample was extracted for 24 h using a mixed solution (250 mL CH_2Cl_2 and 5 mL CH_3OH; boiling temperature of 348.15 K). Finally, after the soxhlet extraction, each sample was tested again by N_2 and CO_2 adsorption.

3.2. NMR analysis

NMR analysis is an advanced method that can be used to analyse shale pore structure and fluid distribution characteristics by using the NMR phenomenon (Brai et al., 2007; Saidian and Prasad, 2015; Xu et al., 2015; Li et al., 2016; Mehana and El-Monier, 2016). Ten bulk samples were saturated with water (mineralisation degree of 20,000 ppm) for 8 h at 25 MPa (Table 2). Then, the pore structure characteristics of the shale were obtained by NMR measurements

Table 1
Samples parameters of gas adsorption and soxhlet extraction.

Sample ID	Depth (m)	Chloroform Bitumen A (%)
L1	2947	0.29
L2	2962	0.27
L3	3025	1.32
L4	3055	1.13
L5	3060	0.77
L6	3105	0.92
L7	3110	0.42
L8	3120	0.62

Note: The data of chloroform bitumen A are obtained from soxhlet extraction.

Table 2
Samples parameters of NMR at water-saturated and manganese-saturated conditions.

Sample ID	Depth (m)	Porosity (%)	Permeability (μD)	S_o
L2	2962	4.88	17.37	59.00
L9	3020	3.31	0.13	70.41
L3	3025	4.15	7.35	77.56
L10	3030	4.41	19.77	70.87
L11	3040	3.37	0.54	17.48
L12	3045	3.68	0.51	17.07
L13	3050	4.24	1.47	17.34
L4	3055	4.29	6.09	15.26
L14	3080	2.61	0.23	19.63
L7	3110	4.13	1.28	16.98

of the water-saturated bulk samples using a nuclear magnetic resonance analyser. The 10 bulk samples were next soaked with manganese chloride aqueous solution (mass fraction of 50%) for one week. The distribution characteristics of the residual hydrocarbon were determined by NMR measurements of the manganese-saturated bulk samples because manganese ions diffuse into the samples and eliminate the NMR signals of hydrogen ions in water.

Three columnar samples with a diameter of 2.5 cm were saturated with kerosene for 24 h at 25 MPa (Table 3). The distribution characteristics of all of the fluids were obtained by NMR measurements in the kerosene-saturated columnar samples. Moreover, the distribution characteristics of movable fluid in the kerosene-saturated columnar samples were then obtained by centrifuge treatment at a speed of 8000 rpm for 4 h.

A columnar sample from the depth of 3042 m was first saturated with kerosene for 24 h at 25 MPa, then the kerosene-saturated columnar sample was displaced with heavy water (no NMR signal). Three pressure points were set up in the process of displacement, 1 MPa, 5 MPa, and 7 MPa, respectively. T_2 spectrums and NMR images were obtained every 15 min at each pressure point. Switching to the next pressure point was then required until there was no obvious difference between the two spectrums. The percolation characteristics of fluid in the process of displacement could be acquired based on the T_2 spectrums and NMR images.

3.3. FE-SEM

FE-SEM is a common method for directly observing the size, shape, and distribution of micro-nano pores and fractures (Jiao et al., 2012; Loucks et al., 2012; Wang et al., 2016). Ar-ion polishing was necessary to reduce the surface roughness of the shale samples. Four samples were polished using a Leica EM TIC 3X Ion Beam Milling System, yielding an approximate polished area of 5 mm × 5 mm. The polished samples were then coated with Au to prevent electrostatic charging. FE-SEM was conducted using secondary electron imagery at an operating current of 10 kV. Each sample was observed using field emission scanning electron microscopy in combination with an energy dispersive X-ray spectrometer.

Table 3
Samples parameters of NMR at kerosene-saturated and centrifugation conditions.

Sample ID	Depth (m)	Porosity (%)	Permeability (μD)	$T_{2cutoff}$ (ms)	S_m (%)
L15	2977	3.75	1.63	10.35	4.88
L16	3035	3.69	4.43	10.00	15.47
L17	3065	3.92	3.74	11.00	8.98

4. Results and discussion

4.1. N_2 adsorption and desorption isotherms

A comparison of the N_2 adsorption isotherms of the samples before and after extraction at liquid nitrogen temperature (77.15 K) is illustrated in Fig. 3. The adsorption amounts of the samples are far larger after extraction than before extraction, indicating that large pore volumes developed in the samples after extraction. The N_2 adsorption isotherms of the samples before and after extraction both show a hysteresis pattern ($P/P_0 > 0.5$) with an absence of a plateau at high relative pressure ($P/P_0 > 0.95$). According to the classification of the International Union of Pure and Applied Chemistry, the N_2 isotherm shapes belong to Type H2 and H3 isotherms (isotherms with a hysteresis loop) (Fig. 4), indicating the existence of ink-bottle-shaped and slit-shaped pores (Sing et al., 1985). Such N_2 isotherm shapes indicate that these materials contain both mesopores, which result in the hysteresis, and macropores, which lead to the absence of a plateau (Kuila et al., 2014). The hysteresis of the samples is more prominent after extraction than before extraction, indicating that more mesopores existed in the samples after extraction than before extraction. The adsorption amounts of the samples after extraction are much greater than those before extraction at the saturated vapour pressure (Fig. 3), indicating that the samples contained more macropores after extraction than before extraction. Additionally, compared with the samples before extraction, almost all the isotherms of the samples after extraction show obvious adsorption at very low relative pressure ($P/P_0 < 0.01$), indicating the existence of micropores.

4.2. Pore structure from CO_2 and N_2 adsorption

Pore structure refers primarily to the pore volume, specific surface area, and PSD, and these parameters as obtained from CO_2 and N_2 adsorption are presented in Table 4 and Figs. 5 and 6. The samples exhibit larger pore volume and specific surface area after extraction than before extraction. The pore volume of the samples after extraction varies from 0.0035 to 0.0159 mL/g, with a mean value of 0.0101 mL/g, which is approximately 2.5 times greater than that of the samples before extraction ranging from 0.0021 to 0.0076 mL/g with a mean value of 0.0040 mL/g (Table 4). The specific surface area of the samples after extraction ranges from 3.17 to 8.68 m^2/g, with an average value of 5.82 m^2/g, which is also approximately 2.5 times greater than that of the samples before extraction ranging from 1.35 to 4.07 m^2/g with an average value of 2.47 m^2/g.

The PSD can be displayed as incremental distribution histograms with respect to pore volume or specific surface area (Clarkson et al., 2013; Tian et al., 2013). As illustrated in Figs. 5 and 6, the different PSD histograms of all the samples before and after extraction are well comparable and display a similar variation trend. The pore volume shows a distinct peak at diameters greater than 10 nm, whereas the specific surface area possesses an obvious

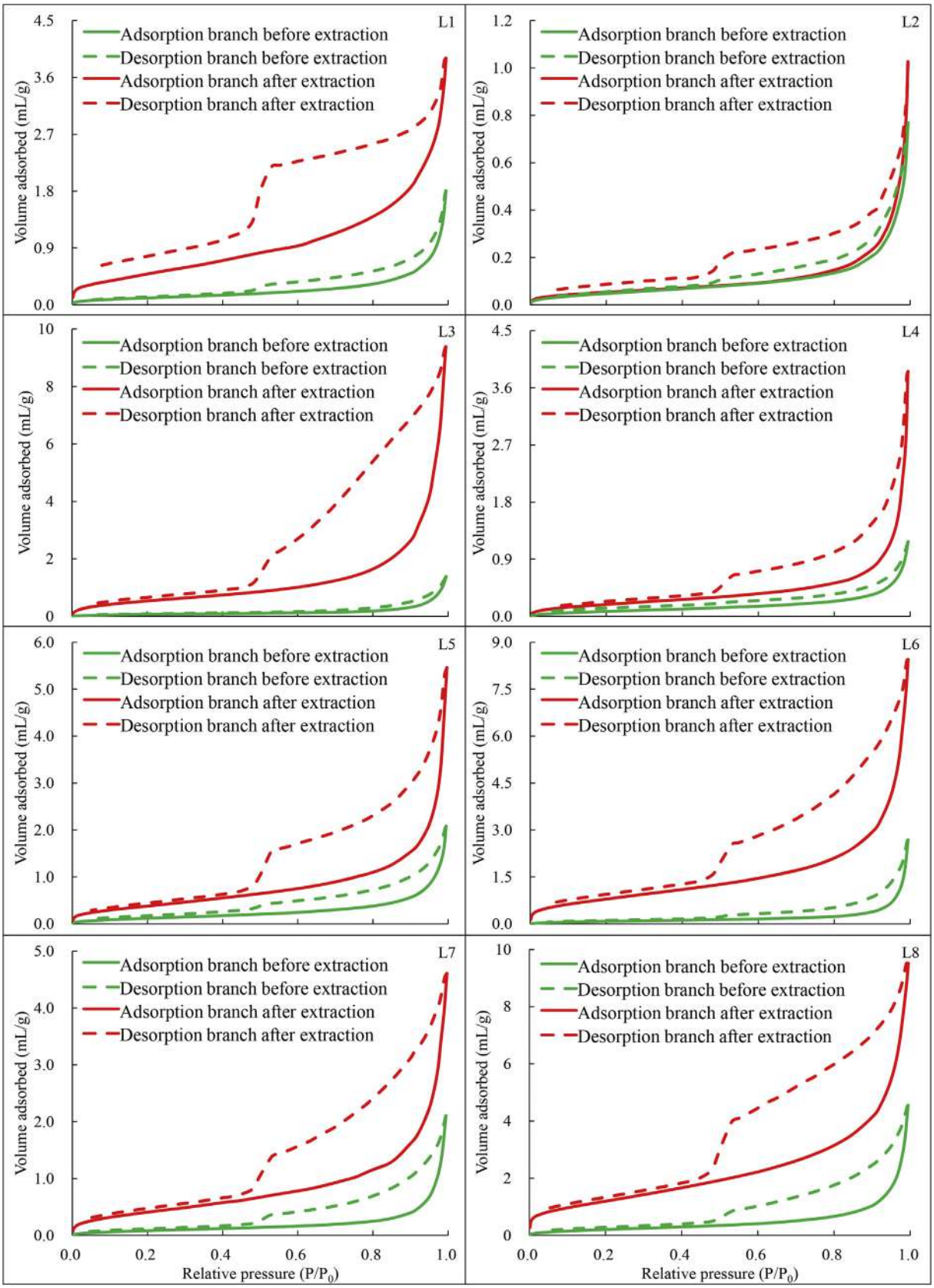

Fig. 3. Comparison of low-pressure N_2 adsorption isotherms of the shale samples before and after extraction at 77.15 K.

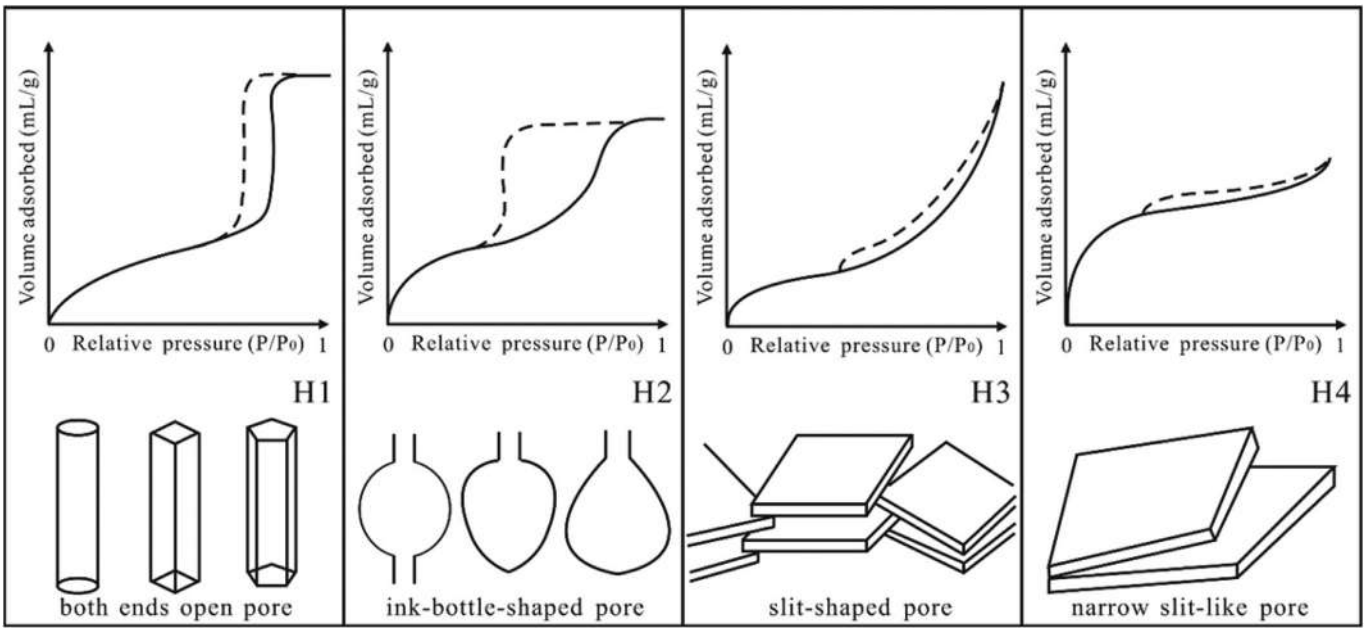

Fig. 4. Types of hysteresis loops and their corresponding pore shapes (modified from Sing et al., 1985).

Table 4
Pore structure parameters of the shale samples from gas adsorption and soxhlet extraction.

Sample ID	Type	Pore volume (mL/g)			Proportion (%)		Specific surface area (m^2/g)			Proportion (%)	
		<10 nm	>10 nm	Total	<10 nm	>10 nm	<10 nm	>10 nm	Total	<10 nm	>10 nm
L1	Before extraction	0.0017	0.0025	0.0042	40.17	59.83	3.87	0.20	4.07	95.02	4.98
	After extraction	0.0038	0.0044	0.0082	46.81	53.19	8.21	0.47	8.68	94.60	5.40
	Increment	0.0022	0.0019	0.0040	53.68	46.32	4.34	0.27	4.61	94.22	5.78
L2	Before extraction	0.0011	0.0011	0.0021	50.30	49.70	2.61	0.09	2.70	96.76	3.24
	After extraction	0.0020	0.0015	0.0035	57.57	42.43	5.40	0.11	5.51	97.96	2.04
	Increment	0.0009	0.0004	0.0013	69.32	30.68	2.79	0.02	2.81	99.12	0.88
L3	Before extraction	0.0006	0.0020	0.0026	23.21	76.79	1.41	0.17	1.58	89.40	10.60
	After extraction	0.0026	0.0132	0.0159	16.52	83.48	4.93	1.25	6.18	79.82	20.18
	Increment	0.0020	0.0112	0.0132	15.19	84.81	3.52	1.08	4.60	76.53	23.47
L4	Before extraction	0.0012	0.0016	0.0028	43.27	56.73	2.93	0.13	3.06	95.74	4.26
	After extraction	0.0016	0.0055	0.0071	22.68	77.32	3.96	0.36	4.32	91.64	8.36
	Increment	0.0004	0.0039	0.0043	9.43	90.57	1.03	0.23	1.26	81.67	18.33
L5	Before extraction	0.0012	0.0029	0.0040	28.98	71.02	2.59	0.23	2.82	91.82	8.18
	After extraction	0.0021	0.0073	0.0094	22.42	77.58	4.21	0.54	4.75	88.58	11.42
	Increment	0.0009	0.0044	0.0054	17.49	82.51	1.62	0.31	1.93	83.85	16.15
L6	Before extraction	0.0006	0.0040	0.0047	13.67	86.33	1.46	0.25	1.71	85.54	14.46
	After extraction	0.0030	0.0108	0.0139	21.90	78.10	5.35	1.00	6.35	84.22	15.78
	Increment	0.0024	0.0068	0.0092	26.09	73.91	3.89	0.76	4.64	83.73	16.27
L7	Before extraction	0.0005	0.0031	0.0036	14.49	85.51	1.12	0.23	1.35	83.22	16.78
	After extraction	0.0017	0.0059	0.0075	22.15	77.85	2.65	0.52	3.17	83.53	16.47
	Increment	0.0011	0.0028	0.0039	29.24	70.76	1.53	0.30	1.83	83.77	16.23
L8	Before extraction	0.0011	0.0065	0.0076	14.41	85.59	1.97	0.51	2.48	79.46	20.54
	After extraction	0.0043	0.0110	0.0152	27.95	72.05	6.49	1.11	7.61	85.35	14.65
	Increment	0.0032	0.0045	0.0076	41.52	58.48	4.52	0.60	5.13	88.20	11.80
Average increment	0.0007	0.0027	0.0033	32.74	67.26	2.23	1.00	3.23	86.39	13.61	

peak at diameters of 0.3–0.9 nm. However, the peak value of the samples is markedly higher after extraction than before extraction.

Moreover, the different PSD histograms with respect to increments of pore volume and specific surface area of the samples before and after extraction also show a similar variation trend (Figs. 5 and 6). Similarly, the volumes of pores with diameters greater than 10 nm increase significantly after the removal of residual hydrocarbon. In contrast, the specific surface area presents a marked increase at diameters of 0.3–0.9 nm. As shown in Table 4, the volume increment of pores with a diameter larger than 10 nm before and after extraction ranges from 0.0004 to 0.0112 mL/g, with an average value of 0.0045 mL/g, which is approximately three times greater than that of pores with a diameter smaller than 10 nm, ranging from 0.0004 to 0.0032 mL/g with an average value of 0.0016 mL/g. Conversely, the specific surface area increment of pores with diameters less than 10 nm before and after extraction ranges from 1.03 to 4.52 m^2/g, with an average of 2.91 m^2/g, which is approximately 6.5 times greater than that of pores with diameters greater than 10 nm, ranging from 0.02 to 1.08 m^2/g with an average of 0.45 m^2/g. This result means that pores with diameters greater than 10 nm provide the main pore volume increment, accounting for 67.26% of the pore volume on average. Conversely, the

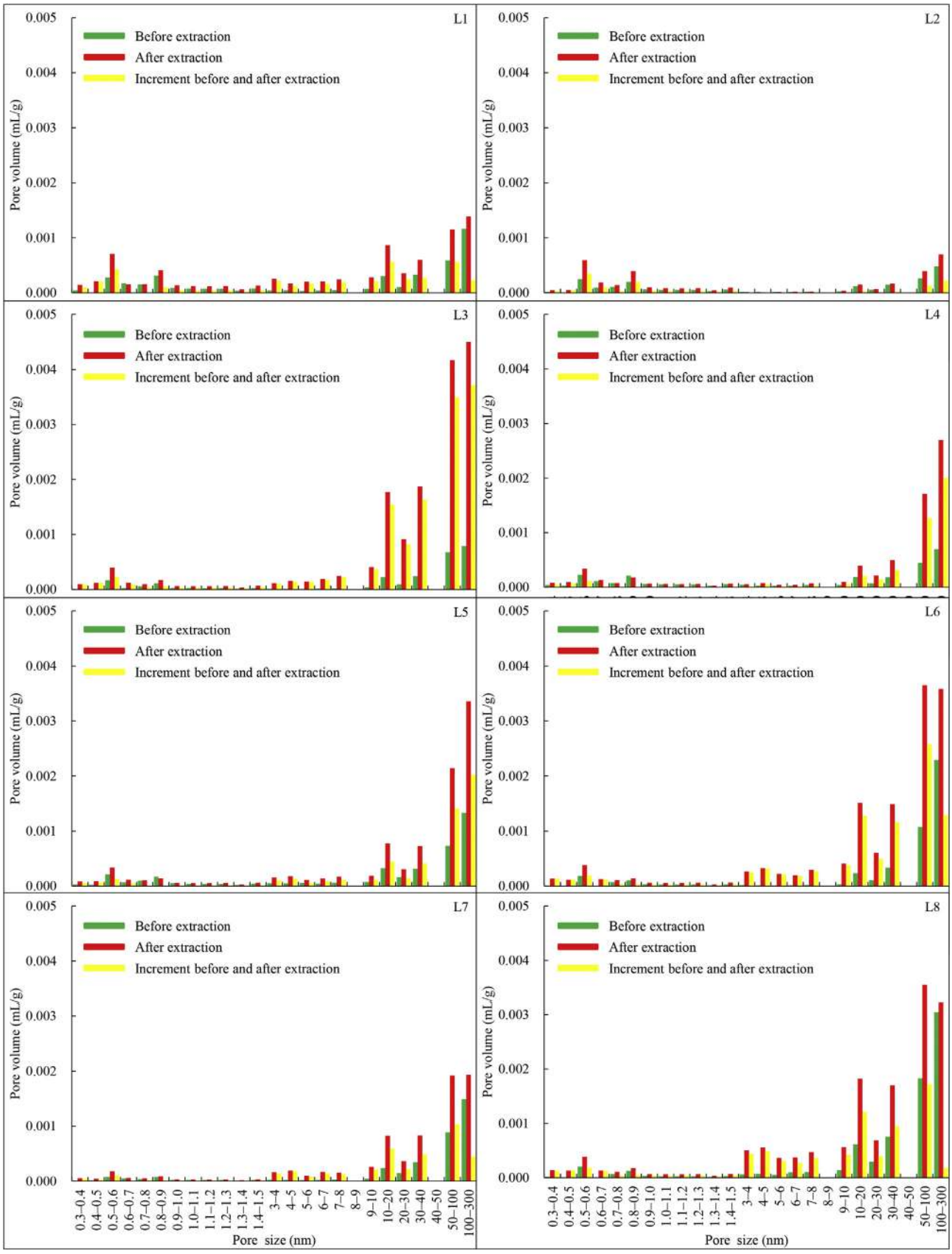

Fig. 5. Comparison of the PSD with respect to pore volume of the shale samples before and after extraction. The data of pores with diameters smaller than 2 nm diameter were obtained from CO_2 adsorption, and the data of pores with diameters larger than 2 nm diameter were obtained from N_2 adsorption.

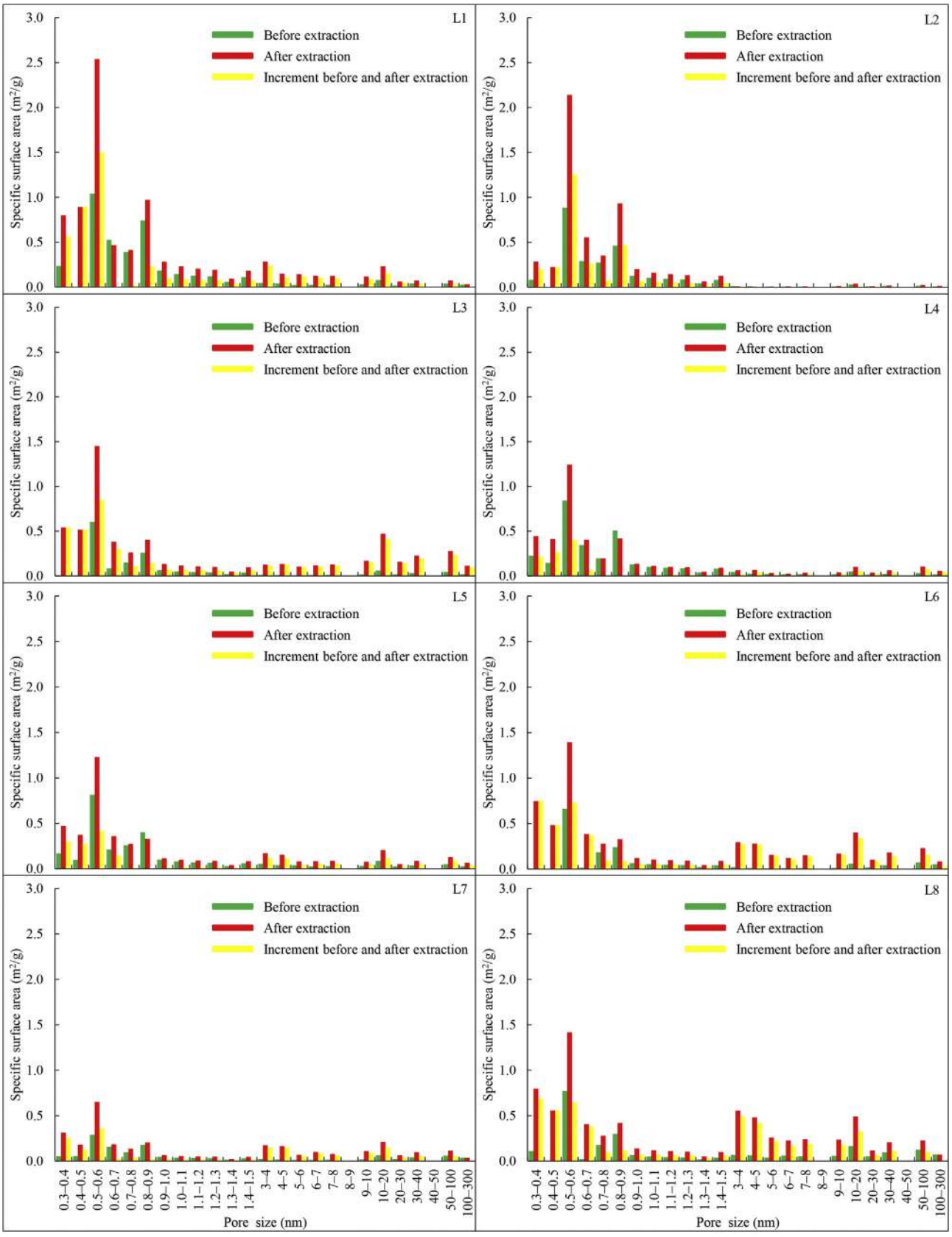

Fig. 6. Comparison of the PSD with respect to specific surface area of the shale samples before and after extraction. The data of pores with diameters smaller than 2 nm diameter were obtained from CO_2 adsorption, and the data of pores with diameters larger than 2 nm diameter were obtained from N_2 adsorption.

specific surface area increment is contributed mainly by pores with diameters smaller than 10 nm, especially those at 0.3–0.9 nm, accounting for 86.39% of the specific surface area on average. This result can be explained by the fact that a large pore can provide a pore volume equal to that of many small pores, whereas a small pore can offer a specific surface area equal to that of many large pores. In addition, oil existing in shale is primarily in the two states of free and adsorbed hydrocarbon. Thus, it is concluded that large pores could provide enough pore volume for free hydrocarbon accumulation and that small pores offer sufficient specific surface area for adsorbed hydrocarbon accumulation.

The significant differences between the samples before and after extraction based on the experimental data of gas adsorption are primarily attributable to the re-exposure of additional pores during the extraction, which means that substantial soluble organic matter remained in the shale samples (Ritter, 2003; Kelemen et al., 2006; Loucks et al., 2009; Curtis et al., 2012; Furmann et al., 2013; Valenza et al., 2013; Guo et al., 2014; Lin et al., 2014; Wei et al., 2014; Ji et al., 2017). As the organic matter in the Es_3^l shale is in the early stage of oil generation, with Ro ranging from 0.70% to 0.91%, the amount of hydrocarbons generated is insufficient to generate enough pressure to promote efficient expulsion of hydrocarbons from the shale. As a result, a portion of hydrocarbons generated remain in the shale. Soluble organic matter in the shale samples occupies a certain amount of pore space (Luo and He, 2014). During the extraction, the hydrocarbon molecules in the shale were dissolved by the organic solvent and carried out of pores, resulting in the change of pore structure, especially the significant growth of pore volume and specific surface area (Pan et al., 2015; Ji et al., 2017). In the N_2 adsorption, because soluble organic matter has the characteristic of being in the solid state at the temperature of 77.15 K, the pore volume occupied by nitrogen molecules was significantly lower in the shale samples before extraction. As a result, the pore volume of the shale samples after extraction obviously increased at diameters greater than 10 nm, indicating that free residual hydrocarbon primarily exists in such pores. In the CO_2 adsorption, most of soluble organic matter was in the liquid state at 273.15 K, and this liquid could dissolve a small amount of carbon dioxide (Pan et al., 2015). However, because of the low relative pressure, the dissolved gas content is so small that it can be disregarded (Zhou et al., 2013). There are two explanations for the increase of specific surface area in the shale samples after extraction. One is that because soluble organic matter in small pores blocks channels for gas diffusion, it is difficult for nitrogen and carbon dioxide molecules under low relative pressure to access these blocked small pores. The other is that soluble organic matter directly attaches to the surface of porous kerogen due to the lipophilicity of kerogen. After removing soluble organic matter, substantial irregular surfaces are directly exposed. Therefore, the removal of soluble organic matter causes substantial small pores to be exposed, especially pores with diameters of 0.3–0.9 nm, so the specific surface area measured by CO_2 adsorption increases significantly, implying that adsorbed residual hydrocarbon occurs primarily in such pores.

Fig. 7 shows the relationship between residual hydrocarbon content and pore structure increments of different grades of pores before and after extraction. The figure shows that no correlation exists between residual hydrocarbon content and pore structure increments of pores with diameters smaller than 10 nm (Fig. 7a and b), whereas residual hydrocarbon content is positively correlated with pore structure increments of pores with diameters greater than 10 nm (Fig. 7c and d), supporting the fact that the residual hydrocarbon content of the samples is primarily controlled by pores with diameters greater than 10 nm. Although the correlation coefficients of residual hydrocarbon content with the pore structure increments of pores with diameters greater than 10 nm are similar, pore volume increment has a more significant control on residual hydrocarbon content, because the linear slope of the pore volume increment is 127 times larger than that of the specific surface area increment (Fig. 7c and d), similarly indicating that most of the residual hydrocarbon occurs in pores with diameters greater than 10 nm in the form of free hydrocarbon.

Admittedly, because it is difficult to extract hydrocarbon within extremely small pores, the accuracy of our experiments may have been influenced by the diameter of the pores. However, extracting oil from extremely small pores is not an easy task for shale oil production, which supports the fact that only free hydrocarbons in large pores with diameters greater than 10 nm are effective resources for shale oil exploration. Therefore, we decided to define pores with diameters smaller than 10 nm as “oil-ineffective pores” and pores with diameters greater than 10 nm as “oil-enriched pores”. Although the statistics of different basins may not be exactly identical because of different geological conditions, it can be concluded that exploring sweet spots with larger pores makes sense for shale oil production.

4.3. Pore structure from NMR at water-saturated and manganese-saturated conditions

Pore types, porosity, permeability and pore structure parameters were analysed based on NMR transverse relaxation time distributions (Kleinberg et al., 1993; Dunn et al., 2002; Yao et al., 2010a, b; Sun et al., 2012; Yu, 2013; Huang et al., 2015; Tan et al., 2015; Xu et al., 2015). NMR measurements were performed to obtain the PSD spectrums at water-saturated and manganese-saturated conditions. Results showed that the PSD spectrums of the shale samples at the water-saturated condition could be divided into two types: unimodal and multimodal PSD spectrums (Fig. 8). The unimodal PSD spectrum has an isolated peak at small pore size, which normally ranges from 1 to 1000 nm (Fig. 8a–d), reflecting well-developed small pores in the samples with diameters smaller than 1000 nm. In contrast, the multimodal PSD spectrum has two or three peaks, and the amplitude of the leftmost peak is much greater than that of the other peaks (Fig. 8e–j), which suggests that not only small pores but also relatively large pores and micro-fractures are well-developed in these samples.

Conversely, all of the PSD spectrums of the shale samples at the manganese-saturated condition present an isolated peak at small pores with diameters of 1–1000 nm, indicating that oil exists primarily in pores with diameters smaller than 1000 nm. Despite this, the PSD spectrums of the shale samples at the manganese-saturated condition also divided into two types. One is a PSD spectrum with a high peak amplitude, corresponding to the unimodal PSD spectrum at the water-saturated condition (Fig. 8a–d). The other is a PSD spectrum with a low peak amplitude, corresponding to the multimodal PSD spectrum at the water-saturated condition (Fig. 8e–j). Although the cumulative amplitudes of the PSD spectrums of all of the shale samples at the water-saturated condition are similar, the cumulative amplitudes of the PSD spectrums at the manganese-saturated condition are markedly different. The samples with the unimodal PSD spectrum at the water-saturated condition show a high cumulative amplitude of PSD spectrum at the manganese-saturated condition, whereas the samples with the multimodal PSD spectrum at the water-saturated condition present a low cumulative amplitude of PSD spectrum at the manganese-saturated condition. In other words, the shale samples with well-developed small pores have high oil saturation (S_o), ranging from 59.00% to 77.56% with an average of 69.46%, whereas the shale samples with well-developed small pores, and relatively large pores and micro-fractures have low oil saturation, varying from 15.56% to 19.63% with an average of 17.29% (Table 2).

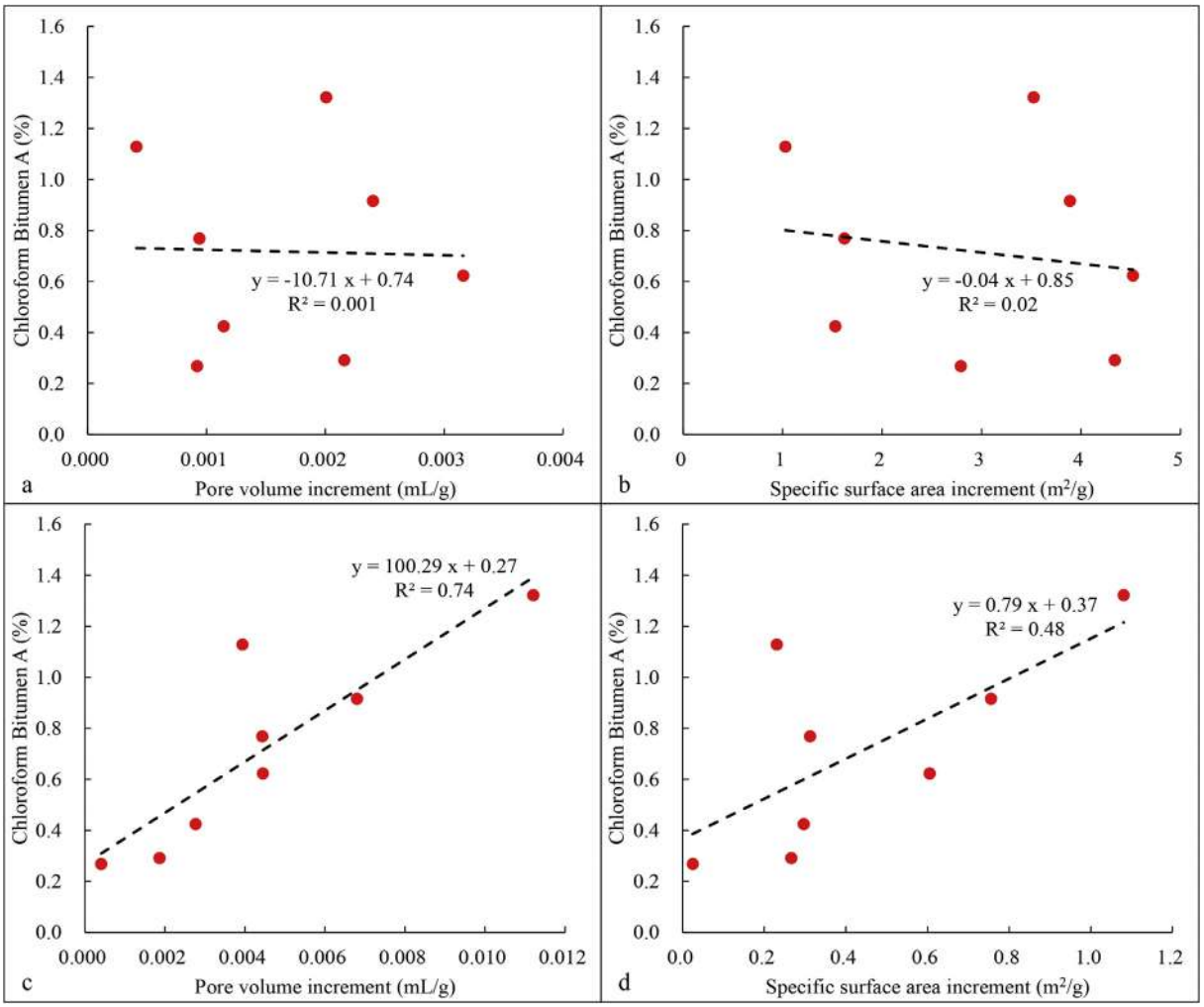

Fig. 7. The relation between residual hydrocarbon content and pore structure increment before and after extraction. a–b: pores with diameters smaller than 10 nm; c–d: pores with diameters larger than 10 nm.

Thus, it can be concluded that the residual hydrocarbon is distributed primarily in pores with diameters smaller than 1000 nm. Pores with diameters smaller than 1000 nm are favourable for hydrocarbon enrichment, whereas pores with diameters greater than 1000 nm are unfavourable for hydrocarbon enrichment. Based on these results, we modify the definition of "oil-enriched pores" stated in the foregoing paragraph to pores with diameters of 10–1000 nm.

4.4. Movable fluid distribution from NMR at kerosene-saturated and centrifugation conditions

NMR measurements were performed at kerosene-saturated and centrifugation conditions, and their corresponding PSD spectrums are illustrated in Fig. 9. The PSD spectrums at the kerosene-saturated condition present a multimodal feature, indicating that small pores, relatively large pores and micro-fractures in the shale samples are all saturated with fluid. However, the peaks of the PSD spectrums are markedly reduced or even vanished after centrifugation. The difference in cumulative amplitude between the PSD spectrums at kerosene-saturated and centrifugation conditions is much greater for large pores than for small pores. The reason for this difference is that fluid in some small closed pores cannot be expelled by centrifugation, whereas fluid in some large pores and micro-fractures with great connectivity can be expelled, which results in the decay of the signal strength and the cumulative amplitude of the PSD spectrum.

We also calculated the NMR transverse relaxation time cutoff value ($T_{2cutoff}$) according to the T_2 spectrums before and after centrifugation. $T_{2cutoff}$ is a relaxation time boundary that divides fluid into two parts, bound fluid and movable fluid, in the T_2 spectrum at the kerosene-saturated condition. Shale samples with a higher bound fluid content must have a greater $T_{2cutoff}$. The calculated NMR $T_{2cutoff}$ values of the samples are shown in Table 3, and these range from 10.00 to 11.00 ms with an average of 10.45 ms, confirming the results of Wang et al. (2001) that indicated that the $T_{2cutoff}$ of a low-permeability reservoir has a wide distribution range with a mean value of 12.85 ms. Therefore, this research reasonably defines the $T_{2cutoff}$ of the shale samples from the study area as 10 ms. Based on the $T_{2cutoff}$, the calculated movable fluid saturation (S_m) of the samples ranges from 4.88% to 15.47%, with an average of 9.78%, and the minimum pore size allowing fluid expulsion under the action of centrifugal force was calculated as 1000 nm. Although large pores with diameters greater than 1000 nm account for only a rather small portion of the total pores, all of the movable fluid exists in such pores and all of the fluid occurring in such pores is movable. Therefore, we herein define pores with a diameter greater than 1000 nm as "oil-percolated

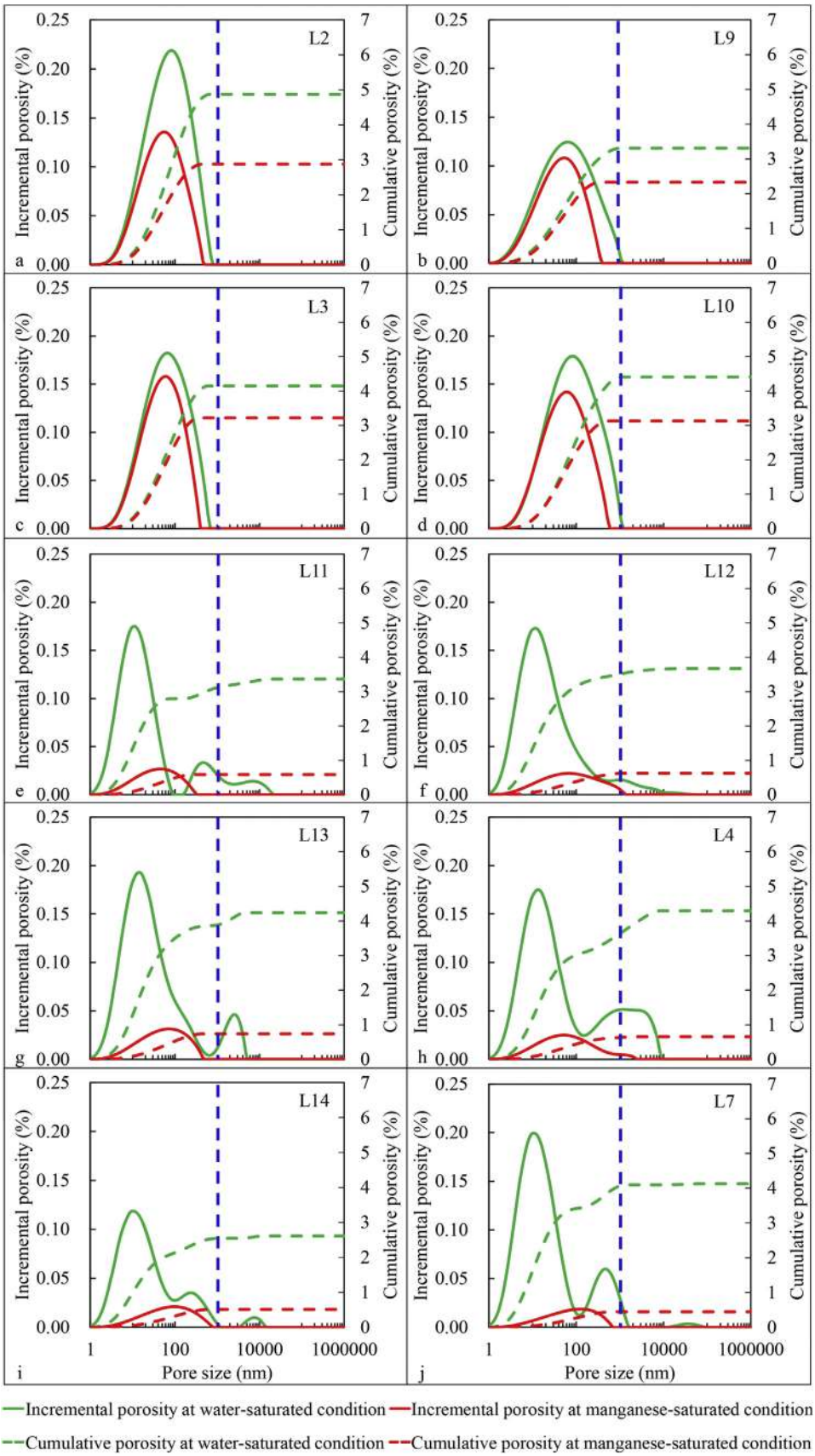

Fig. 8. PSD spectrums of the shale samples from NMR measurements at water-saturated and manganese-saturated conditions.

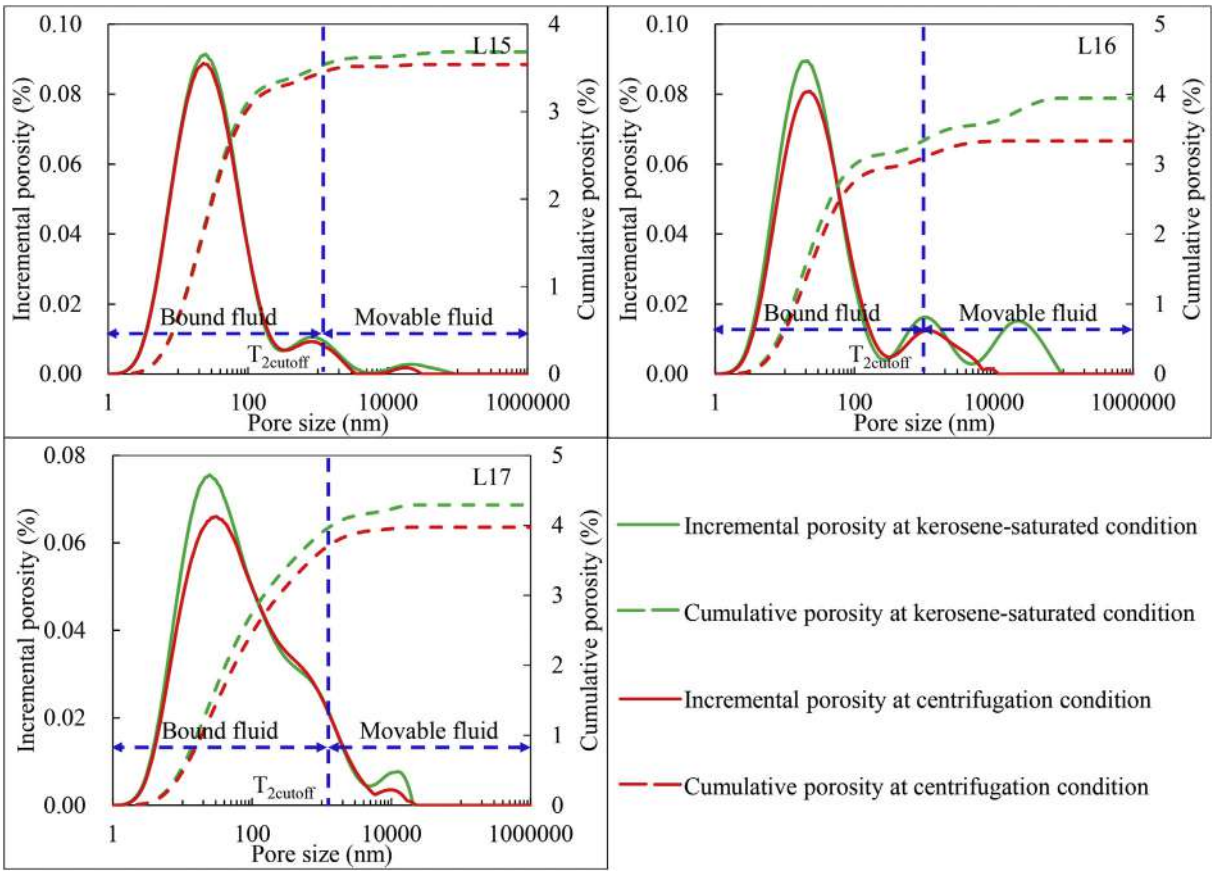

Fig. 9. PSD spectrums of the shale samples from NMR measurements at kerosene-saturated and centrifugation conditions.

pores", which possess great connectivity and are the predominant pathways for hydrocarbon migration and discharge. This is an excellent explanation of why the multimodal PSD spectrums at the water-saturated condition presented a lower peak amplitude at the manganese-saturated condition (Fig. 8). Most of the hydrocarbons that are generated are effectively expelled and cannot accumulate easily, resulting in a low residual hydrocarbon content in the shale samples with well-developed oil-percolated pores. Conversely, pores with a diameter smaller than 1000 nm have poor connectivity and are the primary space for hydrocarbon enrichment. Most of the hydrocarbons generated in these pores cannot be expelled effectively and accumulate easily, resulting in a high residual hydrocarbon content in the shale samples with poorly developed oil-percolated pores.

4.5. Percolation characteristics from NMR at kerosene-saturated and displacement conditions

The percolation characteristics of kerosene in the process of displacement can be acquired based on NMR spectrums and images. As shown by Fig. 10a, the PSD spectrum of the shale sample at the kerosene-saturated condition presents a multimodal feature, reflecting well-developed oil-enriched pores and oil-percolated pores. At the initial kerosene-saturated condition, kerosene is distributed primarily in the oil-enriched pores of the shale sample. With the increase of displacement pressure and time, the spectrum peak of the oil-enriched pores decreases gradually and stabilises to 7 MPa (Fig. 10b–d). However, the spectrum peak of the oil-percolated pores in the process of displacement is apparently higher than that in the initial kerosene-saturated condition, and is characterised by a rightward deviation. Its corresponding displacement process can be observed visually by magnetic resonance imaging, as shown in Fig. 10e–h, in which the colour change from red to blue represents the variation of kerosene content from high to low. At the initial kerosene-saturated condition, kerosene is extensively distributed throughout the shale sample, as shown in Fig. 10e. Subsequently, the kerosene in the shale sample is gradually discharged and eventually presents a localised distribution in the shale sample after displacement, with the final kerosene content accounting for 70% of the initial kerosene content. It can be concluded that with the increase of displacement pressure and time, the heavy water continuously enters the kerosene-saturated shale sample, resulting in kerosene flows from oil-enriched pores to oil-percolated pores and eventually discharges from the shale sample.

4.6. Evidence for the existence of oil-enriched pores and oil-percolated pores from reservoir parameters and FE-SEM

Previous studies have indicated that porosity can be estimated accurately irrespective of mineralogy based on NMR measurements because of the relaxation signal from the hydrogen-containing fluid rather than the matrix in rock (Straley et al., 1997; Coates et al., 1999; Yao et al., 2010a, b). The signal strength of T_2 spectrums at the water-saturated or kerosene-saturated condition can be converted into NMR porosity of shale. The NMR porosity (φ) of the shale samples in this study is within the range of 2.61%–4.88%, with an average of 3.88% (Tables 2 and 3). As a tight reservoir, a shale reservoir is characterised by low permeability. Thus, estimating shale permeability is another important function of the NMR

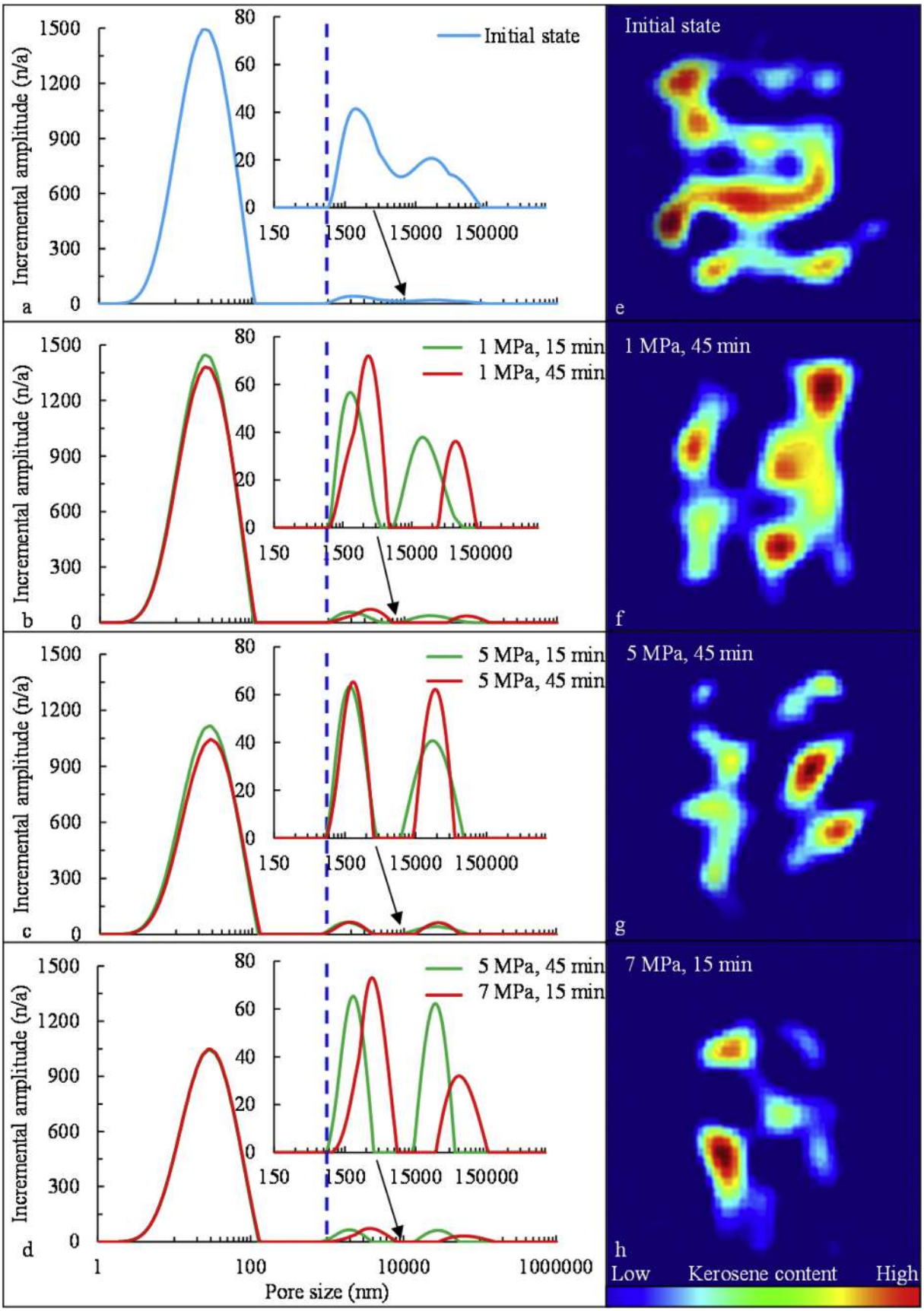

Fig. 10. PSD spectrums and NMR images obtained from NMR measurements at kerosene-saturated and displacement conditions for sample L18 (3042 m).

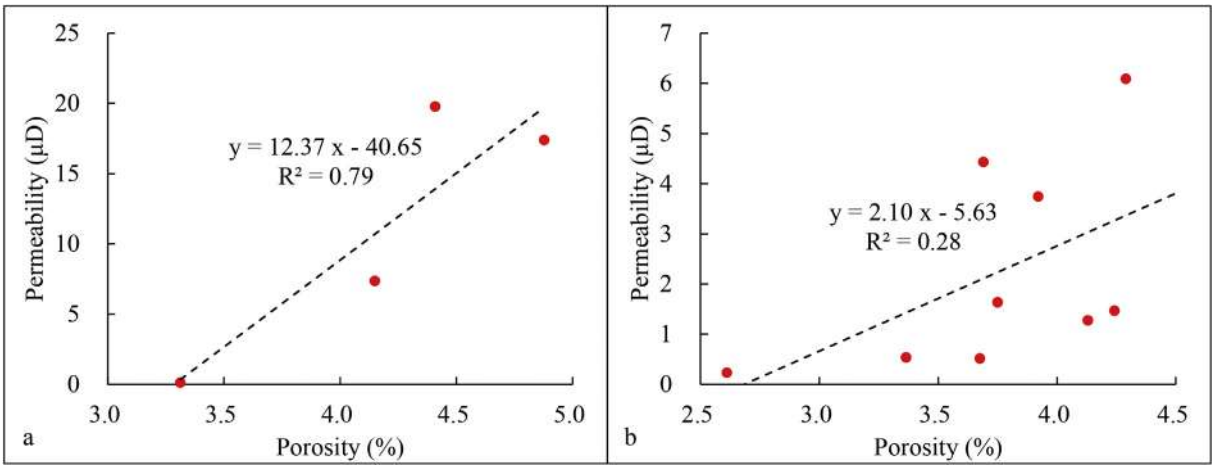

Fig. 11. Relationships between the porosity and permeability of the shale samples from NMR measurements. a: Unimodal shale samples; b: Multimodal shale samples.

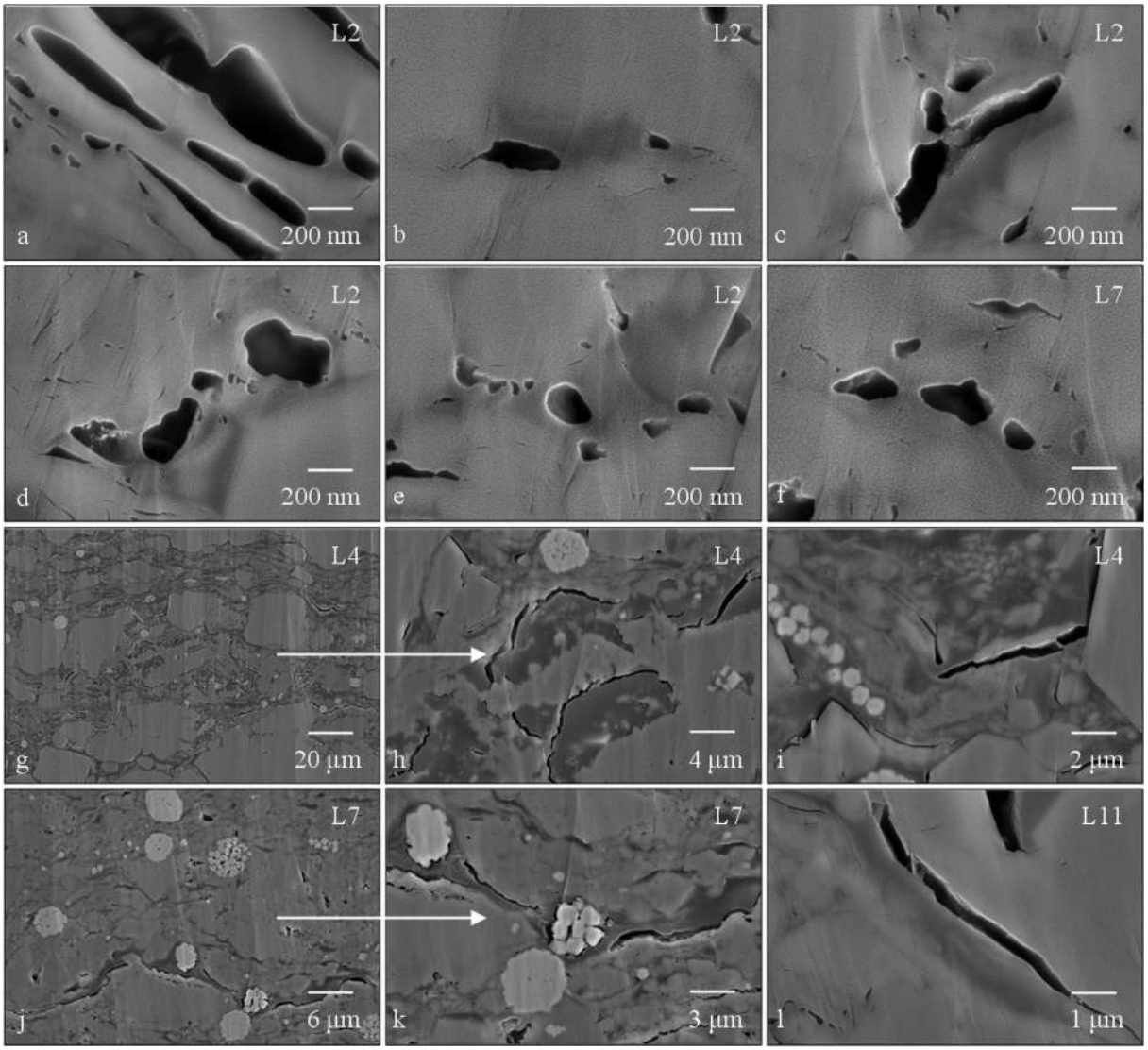

Fig. 12. FE-SEM images of the shale samples. a–f: Spherical and elliptical oil-enriched pores; g–l: Slit-shaped oil-percolated pores.

experiment (Arnold et al., 2006; Shao et al., 2009; Tian, 2010; Ding et al., 2014). The Coates model is a basic model for calculating permeability based on NMR measurements. On the basis of the Timur formula, Coates established the Coates permeability model through a large number of experiments in 1991. See Coates et al. (1991) for detailed information about the calculation. The NMR permeability (κ) of the shale samples in this study is in the range of 0.13–19.77 μD, with an average of 4.97 μD. As is well known, the permeability of small pores has a good relationship with porosity. The greater the porosity is, the greater the permeability is. Conversely, for extremely large pores, especially micro-fractures, there is no good positive correlation between permeability and porosity. A small difference in porosity may be associated with large variation of permeability. In this study, permeability showed a good positive correlation with porosity in four groups of unimodal shale samples (Fig. 11a), indicating that the reservoir space in this type of sample is dominated by small pores (oil-enriched pores) rather than by relatively large pores and micro-fractures. Conversely, permeability showed no apparent relationship with porosity in nine groups of multimodal shale samples (Fig. 11b), indicating that relatively large pores and micro-fractures with great connectivity (oil-percolated pores) are well-developed in this type of samples.

It was also adequately confirmed by FE-SEM observation that spherical and elliptical oil-enriched pores are well-developed in the shale samples (Fig. 12a–f), which is favourable for residual hydrocarbon enrichment. Moreover, slit-shaped oil-percolated pores were observed in the multimodal shale samples (Fig. 12g–l). Large pores and micro-fractures are generally interconnected and may even form a complex fracture mesh, greatly improving the permeability of shale reservoirs and benefitting fluid percolation (Liu et al., 2001; Deng and Liang, 2012; Li et al., 2017b).

5. Conclusions

The effect of pore structure on shale oil accumulation was investigated using both gas adsorption and nuclear magnetic resonance analysis. The findings revealed important information about the effect of pore structure on shale oil accumulation. The conclusions of this study follows.

(1) A large number of ink-bottle-shaped and slit-shaped pores were well-developed in the Es_3^1 shale samples. The samples possessed many more micro–nano pores after extraction than before extraction, especially mesopores and macropores. Moreover, after extraction, the samples exhibited larger pore volume and specific surface area, approximately 2.5 times larger than before extraction.

(2) Pores with diameters larger than 10 nm can provide enough pore volume for free hydrocarbon accumulation, whereas pores with diameters smaller than 10 nm, especially pores with diameters of 0.3–0.9 nm, offer sufficient surface area for adsorbed hydrocarbon accumulation.

(3) Samples with unimodal PSD spectrums at the water-saturated condition, which contained well-developed small pores with diameters smaller than 1000 nm, showed high oil saturation. Conversely, samples with multimodal PSD spectrums at the water-saturated condition, possessing both small pores and also relatively large pores and micro-fractures, showed low oil saturation.

(4) Pores with diameters smaller than 10 nm are considered as “oil-ineffective pores”, whereas pores with diameters of 10–1000 nm are regarded as “oil-enriched pores”. As the minimum pore size allowing fluid expulsion is 1000 nm, pores with diameters larger than 1000 nm are considered as “oil-percolated pores”.

(5) Most of residual hydrocarbon occurs in the form of free hydrocarbon in spherical and elliptical oil-enriched pores and is expelled from shale reservoirs through silt-shaped oil-percolated pores. Large pores and micro-fractures are interconnected and may even form a complex fracture mesh, which greatly improves the permeability of shale reservoirs and is beneficial to fluid percolation.

Acknowledgments

The authors are grateful to all of the editors and anonymous reviewers for their constructive suggestions and comments which significantly improved the manuscript. This study was supported by the National Basic Research Programme of China (973 Project) (No. 2014CB239105). The authors are indebted to the Geoscience Institute of Shengli Oilfield Company, Sinopec, who supplied us with the drill cores and basis data used in this study. The authors also thank Elsevier (webshop.elsevier.com) for the English language review.

References

Arnold, J., Clauser, C., Pechnig, R., Anferova, S., Anferov, V., Blümich, B., 2006. Porosity and permeability from mobile NMR core-scanning. Petrophysics 47, 306–314.
Barrett, E.P., Joyner, L.G., Halenda, P.P., 2014. The determination of pore volume and area distributions in porous substances. I. Computations from nitrogen isotherms. J. Manage. Eng. 24 (4), 207–216.
Brai, M., Casieri, C., Luca, F.D., Fantazzini, P., Gombia, M., Terenzi, C., 2007. Validity of NMR pore-size analysis of cultural heritage ancient building materials containing magnetic impurities. Solid State Nucl. Magn. Reson. 32 (4), 129–135.
Brunauer, S., Emmett, P.H., Teller, E., 1938. Adsorption of gases in multi-molecular layers. J. Am. Chem. Soc. 60 (2), 309–319.
Chalmers, G.R.L., Bustin, R.M., 2007. The organic matter distribution and methane capacity of the Lower Cretaceous strata of Northeastern British Columbia. Can. Int. J. Coal Geol. 70 (1–3), 223–339.
Chalmers, G.R.L., Bustin, R.M., 2008. Lower Cretaceous gas shales in northeastern British Columbia, Part I: geological controls on methane sorption capacity. B. Can. Pet. Geol. 56 (1), 1–21.
Chalmers, G.R.L., Bustin, R.M., Power, I.M., 2012. Characterization of gas shale pore systems by porosimetry, pycnometry, surface area, and field emission scanning electron/transmission electron microscopy image analyses: examples from the Barnett, Woodford, Haynesville, Marcellus, and Doig unit. AAPG Bull. 96 (6), 1099–1119.
Chen, L., Jiang, Z.X., Liu, K.Y., Wang, P.F., Ji, W.M., Gao, F.L., Li, P., Hu, T., Zhang, B., Huang, H.X., 2016. Effect of lithofacies on gas storage capacity of marine and continental shales in the Sichuan Basin, China. J. Nat. Gas. Sci. Eng. 36, 773–785.
Chen, S.B., Zhu, Y.M., Wang, H.Y., Liu, H.L., Wei, W., Fang, J.H., 2011. Shale gas reservoir characterisation: a typical case in the southern Sichuan Basin of China. Energy 36 (11), 6609–6616.
Clarkson, C.R., Solano, N., Bustin, R.M., Bustin, A.M.M., Chalmers, G.R.L., He, L., Blach, T.P., 2013. Pore structure characterization of North American shale gas reservoirs using USANS/SANS, gas adsorption, and mercury intrusion. Fuel 103 (1), 606–616.
Coates, G.R., Peveraro, R.C.A., Hardwick, A., Roberts, D., 1991. The Magnetic Resonance Imaging Log Characterized by Comparison with Petrophysical Properties and Laboratory Core Data. Society of Petroleum Engineers.
Coates, G.R., Xiao, L.Z., Prammer, M.G., 1999. NMR Logging Principles and Applications. Gulf Publishing Company, Houston, Texas.
Cui, X., Bustin, R.M., Brezovski, R., Nassichuk, B., Glover, K., Pathi, V., 2010. A New Method to Simultaneously Measure In-situ Permeability and Porosity under Reservoir Conditions: Implications for Characterization of Unconventional Gas Reservoirs. Society of Petroleum Engineers.
Curtis, J.B., 2002. Fractured shale-gas systems. AAPG Bull. 86 (11), 1921–1938.
Curtis, M.E., Cardott, B.J., Sondergeld, C.H., Rai, C.S., 2012. Development of organic porosity in the Woodford Shale with increasing thermal maturity. Int. J. Coal Geol. 103 (23), 26–31.
De Boer, J.H., Lippens, B.C., 1964. Studies on pore systems in catalysts II. The shapes of pores in aluminum oxide systems. J. Catal. 3 (1), 38–43.
Deng, M.Y., Liang, C., 2012. Studies on reservoir space of mud stone and shale of the lower section of Es3 in Bonan Subsag: an example from Well Luo 69. Earth Sci. Front. 19 (1), 173–181.
Ding, Y.J., Guo, B.H., Yan, X.R., Li, J., Lu, Q., 2014. On identification shale reservoirs validity and physical parameters quantitative evaluation method. Well Logging Technol. 38 (3), 297–303.

Dunn, K.J., Bergman, D.J., Latorraca, G.A., 2002. Petrophysical NMR measurements. Handb. Geophys Explor Seismol. Explor 32, 71–127.
Furmann, A., Mastalerz, M., Brassell, S.C., Schimmelmann, A., Picardal, F., 2013. Extractability of biomarkers from high- and low-vitrinite coals and its effect on the porosity of coal. Int. J. Coal Geol. 107 (5), 141–151.
Guo, H.J., Jia, W.L., Peng, P.A., Lei, Y.H., Luo, X.R., Cheng, M., Wang, X.Z., Zhang, L.X., Jiang, C.F., 2014. The composition and its impact on the methane sorption of lacustrine shale from the Upper Triassic Yanchang Formation, Ordos Basin, China. Mar. Pet. Geol. 57 (2), 509–520.
Guo, X., 2014. Rules of two-factor enrichment for marine shale gas in southern China: understanding from the longmaxi Formation shale gas in Sichuan Basin and its surrounding area. Acta Geol. Sin. 88 (7), 1209–1218.
Haroonabadi, H., Haghifam, M.R., 2013. Characterization of pore systems in seal rocks using nitrogen gas adsorption combined with mercury injection capillary pressure techniques. Mar. Pet. Geol. 39 (1), 138–149.
Huang, J.G., Xu, K.M., Guo, S.B., Guo, H.W., 2015. Comprehensive study on pore structures of shale reservoirs based on SEM, NMR and X-CT. Geoscience 29 (1), 199–205.
Jarvie, D.M., Hill, R.J., Ruble, T.E., Pollastro, R.M., 2007. Unconventional shale-gas systems: the Mississippian Barnett Shale of north-central Texas as one model for thermogenic shale-gas assessment. AAPG Bull. 91 (4), 475–499.
Javadpour, F., Fisher, D., Unsworth, M., 2007. Nanoscale gas flow in shale gas sediments. J. Can. Pet. Technol. 46 (10), 55–61.
Ji, W., Song, Y., Jiang, Z., Chen, L., Li, Z., Yang, X., Meng, M., 2015. Estimation of marine shale methane adsorption capacity based on experimental investigations of Lower Silurian Longmaxi formation in the Upper Yangtze Platform, south China. Mar. Pet. Geol. 68, 94–106.
Ji, W., Song, Y., Jiang, Z., Wang, X., Bai, Y., Xing, J., 2014. Geological controls and estimation algorithms of lacustrine shale gas adsorption capacity: a case study of the Triassic strata in the southeastern Ordos Basin, China. Int. J. Coal Geol. 134, 61–73.
Ji, W., Song, Y., Rui, Z., Meng, M., Huang, H., 2017. Pore characterization of isolated organic matter from high matured gas shale reservoir. Int. J. Coal Geol. 174, 31–40.
Jiang, F., Pang, X., Ouyang, X., Guo, J., Jin, C., Huo, Z., Wang, Q., 2012. The main progress and problems of shale gas study and the potential prediction of shale gas exploration. Earth Sci. Front. 19 (2), 198–211.
Jiao, S., Han, H., Weng, Q., Yang, F., Jiang, D., Cui, L., 2012. Scanning electron microscope analysis of porosity in shale. J. Chin. Electron Microsc. Soc. 31 (5), 432–436.
Kelemen, S.R., Walters, C.C., Ertas, D., Freund, H., Curry, D.J., 2006. Petroleum expulsion part 3. A model of chemically driven fractionation during expulsion of petroleum from kerogen. Energy Fuel. 20 (1), 309–319.
Kleinberg, R.L., Straley, C., Kenyon, W.E., Akkurt, R., Farooqui, S.A., 1993. Nuclear magnetic resonance of rocks: T1 vs. T2. SPE Pap. 26470, 555–563.
Kondo, Seiichi, Ishikawa, Tatsuo, Abe, Ikuo, 2006. Adsorption Technology. Chemical Industry Press of China, Beijing.
Kuila, U., Mccarty, D.K., Derkowski, A., Fischer, T.B., Topór, T., Prasad, M., 2014. Nanoscale texture and porosity of organic matter and clay minerals in organic-rich mudrocks. Fuel 135 (6), 359–373.
Li, A., Ding, W., Wang, R., He, J., Wang, X., Sun, Y., Gu, Y., Jiao, N., 2016. Petrophysical characterization of shale reservoir based on nuclear magnetic resonance (NMR) experiment: a case study of Lower Cambrian Qiongzhusi Formation in eastern Yunnan Province, South China. J. Nat. Gas. Sci. Eng. 37, 29–38.
Li, C., Zhu, X., Zhu, S., Geng, M., Bi, Y., Shu, Q., Xu, F., 2015a. Shale reservoir characteristics of the lower 3th member of Shahejie formation, luojia area, Zhuanhua sag. Acta sedimentol. sin. 33 (4), 795–808.
Li, J., Wang, W., Cao, Q., Shi, Y., Yan, X., Tian, S., 2015b. Impact of hydrocarbon expulsion efficiency of continental shale upon shale oil accumulations in eastern China. Mar. Pet. Geol. 59 (59), 467–479.
Li, T., Jiang, Z., Li, Z., Wang, P., Xu, C., Liu, G., Su, S., Ning, C., 2017a. Continental shale pore structure characteristics and their controlling factors: a case study from the lower third member of the Shahejie Formation, Zhanhua Sag, eastern China. J. Nat. Gas. Sci. Eng. 45, 670–692.
Li, T., Jiang, Z., Xu, C., Yuan, Y., Wang, P., Liu, G., Zhang, B., Ning, C., Wang, Z., 2017b. Effect of sedimentary environment on shale lithofacies in the lower third member of the Shahejie formation, Zhanhua Sag, eastern China. Interpretation 5 (4), 487–501.
Lin, W., Mastalerz, M., Schimmelmann, A., Chen, Y., 2014. Influence of soxhlet-extractable bitumen and oil on porosity in thermally maturing organic-rich shales. Int. J. Coal Geol. 132, 38–50.
Liu, B., Wang, B.S., Ji, W.G., 2001. Closure of micro cracks in rock samples under confining pressure. Chin. J. Geophys. 44 (3), 421–428.
Liu, G., Huang, Z., Chen, F., Jiang, Z., Gao, X., Li, T., Chen, L., Xia, L., Han, W., 2016a. Reservoir characterization of Chang 7 member shale: a case study of lacustrine shale in the Yanchang Formation, Ordos Basin, China. J. Nat. Gas. Sci. Eng. 34, 458–471.
Liu, G., Huang, Z., Jiang, Z., Chen, J., Chen, F., Xing, J., 2016b. Gas adsorption capacity calculation limitation due to methane adsorption in low thermal maturity shale: a case study from the Yanchang Formation, Ordos basin. J. Nat. Gas. Sci. Eng. 30, 106–118.
Liu, H., Zhang, S., Wang, P., Wang, W., Zhu, R., Liu, H., 2012. Lithofacies characteristics of Lower Es3 shale in Luojia area, Zhanhua Sag. PGRE 19 (6), 11–15.
Loucks, R.G., Reed, R.M., Ruppel, S.C., Hammes, U., 2012. Spectrum of pore types and networks in mudrocks and a descriptive classification for matrix-related mudrock pores. AAPG Bull. 96 (6), 1071–1098.
Loucks, R.G., Reed, R.M., Ruppel, S.C., Jarvie, D.M., 2009. Morphology, genesis, and distribution of nanometer-scale pores in siliceous mudstones of the Mississippian Barnett Shale. J. Sediment. Res. 79 (12), 848–861.
Luo, J., He, Y., 2014. Characteristics of the permian source rocks in the middle and upper yangtze region. Nat. Gas. Geosci. 25 (9), 1416–1425.
Mastalerz, M., Schimmelmann, A., Drobniak, A., Chen, Y., 2013. Porosity of Devonian and Mississippian New Albany Shale across a maturation gradient: insights from organic petrology, gas adsorption, and mercury intrusion. AAPG Bull. 97 (10), 1621–1643.
Mehana, M., El-Monier, I., 2016. Shale characteristics impact on nuclear magnetic resonance (NMR) fluid typing methods and correlations. Petroleum 2 (2), 138–147.
Montgomery, S.L., Jarvie, D.M., Bowker, K.A., Pollastro, R.M., 2005. Mississippian Barnet Shale, Fort Worth Basin, north-central Texas: gas-shale play with muti-trillion cubic foot potential. AAPG Bull. 89 (2), 155–175.
Pan, L., Xiao, X., Zhou, Q., 2015. Fluence of soluble organic matter on characterization of shale reservoir. Nat. Gas. Geosci. 26 (9), 1729–1936.
Ritter, U., 2003. Solubility of petroleum compounds in kerogen: implications for petroleum expulsion. Org. Geochem 34 (3), 319–326.
Ross, D.J.K., Bustin, R.M., 2007. Shale gas potential of the lower jurassic gordondale member, northeastern british columbia, Canada. Bull. Can. Pet. Geol. 55 (1), 51–75.
Ross, D.J.K., Bustin, R.M., 2008. Characterizing the shale gas resource potential of Devonian-Mississippian strata in the Western Canada sedimentary basin: application of an integrated formation evaluation. AAPG Bull. 92 (1), 87–125.
Ross, D.J.K., Bustin, R.M., 2009. The importance of shale composition and pore structure upon gas storage potential of shale gas reservoirs. Mar. Pet. Geol. 26 (6), 916–927.
Rouquerol, J., Avnir, D., Fairbridge, C.W., Everett, D.H., Haynes, J.H., Pernicone, N., Ramsay, J.D.F., Sing, K.S.W., Unger, K.K., 1994. Recommendations for the characterization of porous solids. Pure Appl. Chem. 66 (8), 1739–1758.
Saidian, M., Prasad, M., 2015. Effect of mineralogy on nuclear magnetic resonance surface relaxivity: a case study of Middle Bakken and Three Forks formations. Fuel 161, 197–206.
Shao, W.Z., Ding, Y.J., Liu, Y., Liu, S.Q., Li, Y.Q., Zhao, J.H., 2009. The application of NMR log data in evaluation of reservoir pore structure. Well Logging Technol. 33 (1), 52–56.
Sing, K.S., Everett, D.H., Haul, R.A.W., Moscou, L., Pierotti, R.A., Rouquerol, J., Siemieniewsha, T., 1985. Reporting physisorption data for gas/solid systems with special reference to the determination of surface area and porosity. Pure Appl. Chem. 57 (4), 603–619.
Song, G., Xu, X., Li, Z., Wang, X., 2015. Factors controlling oil production from Paleogene shale in Jiyang depression. Oil Gas Geol. 36 (3), 463–471.
Song, M., Zhang, S., Wang, Y., Shi, D., Meng, T., 2011. Lithology classification and prediction of favorable areas of Sha III mudstone-fractured reservoir in Zhanhua depression. PGRE 18 (6), 18–22.
Straley, C., Rossini, D., Vinegar, H., Tutunjian, P., Morriss, C., 1997. Core analysis by low field NMR. Log. Anal. 38 (2), 84–93.
Sun, J.C., Chen, J.P., Yang, Z.M., Liu, X.W., Liu, Y.J., 2012. Experimental study of the NMR characteristics of shale reservoir rock. Sci. Technol. Rev. 30 (14), 25–30.
Tan, M.J., Mao, K.Y., Song, X.D., Yang, X., Xu, J.J., 2015. NMR petrophysical interpretation method of gas shale based on core NMR experiment. J. Pet. Sci. Eng. 136, 100–111.
Tang, X., Jiang, Z., Jiang, S., Wang, P., Xiang, C., 2016. Effect of organic matter and maturity on pore size distribution and gas storage capacity in high-mature to post-mature shales. Energy Fuel 30 (11), 8985–8996.
Tian, H., Pan, L., Xiao, X.M., Wilkins, R.W.T., Meng, Z.P., Huang, B.J., 2013. A preliminary study on the pore characterization of Lower Silurian black shales in the Chuandong Thrust Fold Belt, southwestern China using low pressure N2 adsorption and FE-SEM methods. Mar. Pet. Geol. 48, 8–19.
Tian, H., Zhang, S., Liu, S., Zhang, H., 2012. Determination of organic-rich shale pore features by mercury injection and gas adsorption methods. Acta Pet. Sin. 33 (3), 419–427.
Tian, Y., 2010. NMR logging permeability models and application. Inn. Mong. Petrochem. Ind. 10, 25–27.
Valenza, J.J., Drenzek, N., Marques, F., Pagels, M., Mastalerz, M., 2013. Geochemical controls on shale microstructure. Geology 41 (5), 611–614.
Wang, H., Hu, T., 2014. Analysis of influence factors of shale oil formation in Zhuanhua depression of Bohai Bay Basin. Nat. Gas. Geosci. 25 (1), 141–149.
Wang, P., Jiang, Z., Ji, W., Zhang, C., Yuan, Y., Chen, L., Yin, L., 2016. Heterogeneity of intergranular, intraparticle and organic pores in Longmaxi shale in Sichuan Basin, South China: evidence from SEM digital images and fractal and multifractal geometries. Mar. Pet. Geol. 72, 122–138.
Wang, S., 2009. Analysis of rock pore structural characteristic by nuclear magnetic resonance. Xinjiang Pet. Geol. 30 (6), 768–770.
Wang, W.M., Ye, Z.H., Guo, H.K., 2001. Experimental studies of NMR properties of continental sedimentary rocks. Chin. J. Magn. Reson 18 (2), 113–121.
Wang, Y., Li, Z., Gong, J., Zhu, J., Hao, Y., Hao, X., Wang, Y., 2013b. Discussion on an evaluation method of shale oil and gas in Jiyang depression: a case study on Luojia area in Zhanhua Sag. Acta Pet. Sin. 34 (1), 83–91.
Wang, Y., Wang, W., Hao, Y., 2013a. Shale reservoir characteristics analysis of the Paleogene Shahejie formation in luojia area of Zhanhua Sag, Jiyang depression. J. Palaeogeogr. 15 (5), 657–662.
Wang, Z., 2015. Breakthrough of Fuling shale gas exploration and development and

its inspiron. Oil Gas Geol. 36 (1), 1–6.
Wei, L., Mastalerz, M., Schimmelmann, A., Chen, Y., 2014. Influence of Soxhlet extractable bitumen and oil on porosity in thermally maturing organic-rich shales. Int. J. Coal Geol. 132, 38–50.
Xiong, F., Jiang, Z., Chen, J., Wang, X., Huang, Z., Liu, G., Chen, F., Li, Y., Chen, L., Zhang, L., 2016. The role of the residual bitumen in the gas storage capacity of mature lacustrine shale: a case study of the Triassic Yanchang shale, Ordos Basin, China. Mar. Pet. Geol. 69, 205–215.
Xu, H., Tang, D., Zhao, J., Li, S., 2015. A precise measurement method for shale porosity with low-field nuclear magnetic resonance: a case study of the Carboniferous–Permian strata in the Linxing area, eastern Ordos Basin, China. Fuel 143, 47–54.
Yao, Y.B., Liu, D.M., Cai, Y.D., Li, J.Q., 2010a. Advanced characterization of pores and fractures in coals by nuclear magnetic resonance and X-ray computed tomography. Sci. China-Earth Sci. 53 (6), 854–862.
Yao, Y.B., Liu, D.M., Yao, C., Tang, D.Z., Tang, S.H., Huang, W.H., 2010b. Petrophysical characterization of coals by low-field nuclear magnetic resonance (NMR). Fuel 89 (7), 1371–1380.
Yu, B.S., 2013. Classification and characterization of gas shale pore system. Earth Sci. Front. 20 (4), 211–220.
Zhang, F., Wang, W., Zhang, J., Li, B., 2005. Controlling of faults on sedimentation in Zhanhua Sag. J. Univ. Petroleum, China 29 (5), 1–6.
Zhao, M., Fu, A., Guan, L., Wang, M., Zhu, J., 2012. Logging evaluation method of shale oil and gas reservoir in Luojia area. PGRE 19 (6), 20–24.
Zhou, Q., Tian, H., Chen, G., Hu, J., 2013. Geological model of dissolved gas in pore water of gas shale and its controlling factors. J. China Coal Soc. 38 (5), 800–804.